ASME Journal of Mechanisms and Robotics
Online journal at:
https://asmedigitalcollection.asme.org/mechanismsrobotics

Michael Clancy
Surgical Robotics Laboratory,
Department of Biomedical Engineering,
Rowan University,
201 Mullica Hill Road,
Glassboro, NJ 08028
e-mail: clancym1@rowan.edu

Fayez Alruwaili
Surgical Robotics Laboratory,
Department of Biomedical Engineering,
Rowan University,
201 Mullica Hill Road,
Glassboro, NJ 08028
e-mail: alruwa16@rowan.edu

Marzieh S. Saeedi-Hosseiny
Surgical Robotics Laboratory,
Department of Biomedical Engineering,
Rowan University,
201 Mullica Hill Road,
Glassboro, NJ 08028
e-mail: saeedi64@rowan.edu

Sean McMillan
School of Osteopathic Medicine,
Rowan University,
113 E Laurel Road,
Stratford, NJ 08084
e-mail: smcmillan@virtua.org

Iulian I. Iordachita
Mem. ASME
Laboratory for Computational Sensing and Robotics,
Johns Hopkins University,
3400 N Charles Street,
Baltimore, MD 21218
e-mail: iordachita@jhu.edu

Mohammad H. Abedin-Nasab[1]
Surgical Robotics Laboratory,
Department of Biomedical Engineering,
Rowan University,
201 Mullica Hill Road,
Glassboro, NJ 08028
e-mail: abedin@rowan.edu

Analysis and Optimization of a 6-DoF 3-RRPS Parallel Mechanism for Robot-Assisted Long-Bone Fracture Surgery

Robot-assisted femur repair has been of increased interest in recent literature due to the success of robot-assisted surgeries and current reoperation rates for femur fracture surgeries. The current limitation of robot-assisted femur fracture surgery is the lack of large force generation and sufficient workspace size in traditional mechanisms. To address these challenges, our group has created a 3-RRPS parallel mechanism, Robossis, which maintains the strength of parallel mechanisms while improving the translational and rotational workspace volume. In this paper, an optimal design methodology of parallel mechanisms for application to robot-assisted femur fracture surgery using a single-objective genetic algorithm is proposed. The genetic algorithm will use a single-objective function to evaluate the various configurations based on the clinical and mechanical design criteria for femur fracture surgery as well as the global conditioning index. The objective function is composed of the desired translational and rotational workspaces based on the design criteria, dynamic load-carrying capacity, and the homogeneous Jacobian global conditioning index. Lastly, experimental results of Robossis were obtained to validate the kinematic solution and the mechanism itself; Robossis had an average error of 0.31 mm during experimental force testing. [DOI: 10.1115/1.4063167]

Keywords: parallel mechanism, optimization, genetic algorithm, mechanism design, femur fractures, robot-assisted surgery, medical robotics

1 Introduction

The need for improved clinical outcomes, both intraoperative and postoperative, combined with the ever-advancing field of medical research, has brought surgical robotics to the forefront of surgical innovation [1]. Recently, robotic-assisted surgeries have been shown to decrease costs, improve recovery times, and improve

[1]Corresponding author.
Contributed by the Mechanisms and Robotics Committee of ASME for publication in the Journal of Mechanisms and Robotics. Manuscript received March 3, 2023; final manuscript received August 5, 2023; published online August 29, 2023. Assoc. Editor: Chin-Hsing Kuo.

patient outcomes [2,3]. These affirmative clinical outcomes coupled with the rise in fractures since the turn of the century have motivated research on robot-assisted fracture reduction and alignment surgeries. Femur fracture surgeries have been of particular interest, primarily due to undesirable clinical outcomes. The 1-year mortality rate for persons ≥50 is 25%, 21%, and 20% for proximal, shaft, and distal femur fractures, respectively. For males ≥50, the proximal femur fracture mortality rate is 32% [4]. A significant factor in this is the postoperative malalignment rate and the need for reoperation. The torsional malalignment rate for all femoral fractures has been reported up to 27.5%, where malalignment is defined as >5 deg of angulation in any coordinate plane [5]. These high rates of malalignment and 1-year mortality suggest that it is necessary to improve surgical procedure efficacy and patient outcomes for femur fractures.

During the surgical procedure for femur fracture repair, the reduction of fragments poses significant challenges. The difficulties associated with the reduction and alignment of these fractures are due to the complex anatomy of the femur and the significant passive muscle forces of the thigh (maximal recorded forces: 504.7 N and 38.3 Nm) [6].

Robot-assisted orthopedic trauma surgery is a developing field of research. This field aims to provide surgeons with techniques that allow for high precision and high force generation in the operating room. Despite the growing field, traditional and current mechanisms have not been shown to be capable of opposing the large forces observed during long-bone fracture reduction while maintaining a sufficiently large translational and rotational workspace. Table 1 illustrates the various parallel mechanisms that have been used for robot-assisted femur fracture surgery, their maximal load, and range of motion.

To address these load and workspace challenges, our group previously presented Robossis, a novel design of a 3-RRPS 6-degree-of-freedom (DoF) parallel mechanism, and has completed a comprehensive theoretical analysis, including the derivation of the inverse and forward kinematics, Jacobian via the theory of screws, and inverse dynamics. In addition, our group conducted an investigation into the kinematic and dynamic performance, focusing on singularity, force transmission, Jacobian, and performance index analysis [18–21] as well as preliminary benchtop and cadaver testing [22–25].

For the application of femur fractures, the size of the translational and rotational workspaces is an important indicator of the performance of a parallel mechanism. Based on the literature available, we used the reported femur fracture malalignment ranges to quantify certain translational and rotational ranges a mechanism must satisfy to be considered a viable solution for robot-assisted femur fracture surgery. We compared the workspace viability of Robossis alongside the traditional Gough–Stewart platform (GSP).

Table 1 Parallel mechanisms used for femur fracture reduction

Year	Type	Max. load (N)	Range of motion
2004 [7]	P, GSP	NR	NR
2013 [8]	P, GSP	NR	NR
2012 [9]	S-P-H	600 N	$x \pm 75$ mm, ±30 deg $y \pm 100$ mm, ±15 deg $z \pm 75$ mm, ±30 deg
2008 [10]	P	260 N	$x \pm 100$ mm, ±10 deg $y \pm 200$ mm, ±35 deg $z \pm 100$ mm, ±10 deg
2013 [11]	P, GSP	NR	NR
2014 [12]	P, GSP	2460 N	NR
2017 [13]	P, GSP	1243 N	$x \pm 220$ mm, ±43 deg z 20–250 mm, ±35 deg $y \pm 95$ mm, ±130 deg
2016 [14]	S-P-H	147 N	NR
2020 [15]	P, 3RRPS	NR	$x \pm 120$ mm, [−15 deg, 18 deg] y [−138 mm, 106 mm], ±183 deg z [235 mm, 375 mm], ±180 deg
2020 [16]	P, GSP	500 N	NR
2022 [17]	P, GSP	561 N	NR

Note: P: parallel; S: serial; H: hybrid; GSP: Gough–Stewart platform; NR: not reported.

In this paper, we propose an optimal design methodology of parallel mechanisms for application to robot-assisted femur fracture surgery using a single-objective genetic algorithm. The genetic algorithm will use an objective function to evaluate the various configurations based on the clinical and mechanical design criteria as well as the homogenous Jacobian global conditioning index (GCI). Additionally, we demonstrate the performance of Robossis through force and position testing to validate the inverse kinematic solution.

2 Clinical and Mechanical Requirements

One of the significant and impactful complications in femur repair is the malrotation of the femur fragments. Regardless of the location of the fracture, proximal, shaft, or distal, there is no less than a 24% reported malrotation rate [5,26,27]. These malrotations have been shown to alter a person's gait and quality of life [28].

In part, the reason a surgical robot has not yet seen widespread clinical use is due to the clinical and mechanical design requirements necessary for use in the operating room. A surgical robot designed for long-bone femur fracture surgeries is required to meet or exceed the required accuracy, rotational and translational movements, and maximal forces observed during the procedure. The required accuracy is derived from the Thoresen metric [29]. The highest score on the Thoresen metric, "Excellent," is defined as alignment within ±1 cm and ±5 deg. A goal of this work is to show that Robossis can perform at least 50% better than the Thoresen "Excellent" metric of ±0.5 cm and ±2.5 deg.

To understand the maximal forces present during femur fracture repair, Zhu et al. measured the intraoperative passive muscle forces along the anatomical axes. The maximal anterior–posterior (AP), medial–lateral (ML), and femoral–shaft (FS) forces were 472.4, 203.0, and 504.7 N, respectively [6]. Zhu et al. reported maximal torques for the anterior–posterior and medial–lateral axes of 16.4 Nm and 38.3 Nm, respectively. Estimated forces from pressure readings were not included in Table 2.

In addition to the mechanical requirements of force and torque, there are clinical criteria that focus on the usability of the design. It is desired to have a surgical robot that can be used with all patient body types. McDowell et al. [30] reported the average male center thigh circumference as 53.8 cm ± 9.13 cm. Robossis, with a ring circumference greater than 81.1 cm (radius greater than 12.9 cm, Table 2), can be used with 99.7%, 3 standard deviations, of all patient body types.

Furthermore, the femur fracture malalignment range was determined to provide a preliminary approximation of the translations and rotations necessary for femur fractures. The required rotations were derived from the maximal reported malrotations for the AP, ML, and FS axes [27,31]. The required translations along the FS were derived from the maximal reported leg length discrepancy reported by Citak et al. [32]. Lowe et al. studied cadaveric femur fractures and found a medial and anterior translation of 17.1 mm ± 10.4 mm and 6.0 mm ± 4.3 mm, respectively, when reducing the fractures [33]. Using three standard deviations gives a maximal medial and anterior translation of 48.3 mm and 18.9 mm, respectively. These values are the femur fracture malalignment range listed in Table 2.

3 Robossis Architecture

The 6-DoF 3-RRPS parallel mechanism, Robossis, is shown in Fig. 1. The design is a three-arm parallel mechanism, with each arm affixed to both a moving and stationary ring using spherical and universal joints, respectively. The proposed application of Robossis is shown in Fig. 2. Robossis will be placed over the lower leg to allow clinicians access to the fracture surgical area. Surgical Schanz screws will be used to attach Robossis to the distal

Table 2 Clinical and mechanical requirements and femur fracture malalignment range for a long-bone femur fracture robot

Parameter	Mechanical requirement		
Accuracy [29]	±1 cm, ± 5 deg		
	Anterior–posterior axis	Medial–lateral axis	Femoral–shaft axis
Load [6]	472.4 N	203.0 N	504.7 N
Torque [6,34]	16.4 Nm	38.3 Nm	39 Nm
	Clinical requirement		
Ring size	>12.9 cm [30]		
	Femur fracture malalignment range		
	Anterior–posterior axis	Medial–lateral axis	Femoral–shaft axis
Translations [32,33]	±1.89 cm	±4.83 cm	± 5.4 cm
Rotations [27,31]	±10.3 deg	±8.1 deg	±42.0 deg

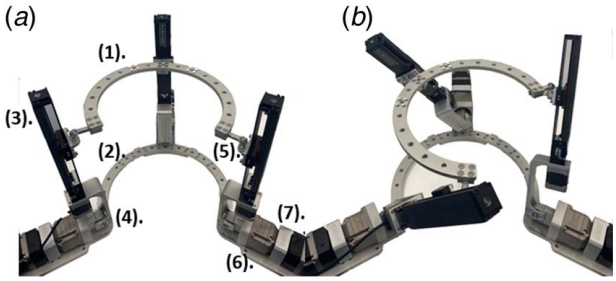

Fig. 1 Constructed mechanism in (*a*) the neutral position and (*b*) the maximal rotation position (~45 deg): (1) the moving ring, (2) the fixed ring, (3) linear slide actuator, (4) the universal joint connects the gearbox to the lower arm, (5) spherical joint, (6) gearbox, and (7) stepper motor

fracture (Fig. 2(2)). The robot will be attached after traction is pulled to eliminate large variances in the femoral–shaft axis (z-axis).

Robossis is actuated by two types of Autonics stepper motors. Affixed to the stationary ring are three Autonics-A8K (Busan, South Korea) stepper motors with a nominal holding torque of 0.814 Nm. The A8K motors are coupled with a 60:1 gearbox to increase the output to 48.6 Nm. Each arm consists of a HIWIN-KK40 (Hiwin, Taichung, Taiwan) linear actuator with a 1 mm pitch. The linear actuator is

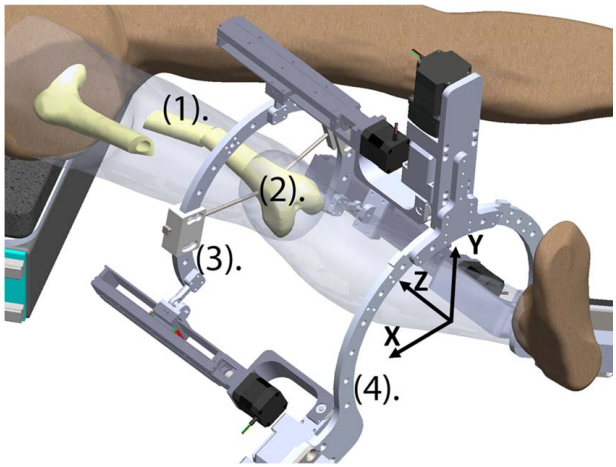

Fig. 2 Proposed use case of Robossis for robot-assisted long-bone fracture surgery: (1) shaft femur fracture, (2) Schanz screws attach the distal femur fragment to the moving ring, (3) moving ring (*h*), and (4) fixed ring (*g*)

powered by an Autonics-A3K (Busan, South Korea) stepper motor, nominal holding torque = 0.235 Nm. Assuming a torque-to-force efficiency of 0.9, the maximal linear force generated is 1527 N for each arm, for a total theoretical load insertion of 4581 N.

4 Inverse Kinematics

Based on the 6-DoF position of the end effector, $P(x, y, z, \alpha, \beta, \gamma)$, the linear actuator length (d_i) and active joint angle (θ_i) are calculated. Referring to Fig. 3(*a*), signifying a_i and b_i (representing OA_i and PB_i) in reference frame {A}, it can be determined that

$$\boldsymbol{r_i} - \boldsymbol{a_i} = \boldsymbol{p} + \boldsymbol{b_i} - \boldsymbol{a_i} \tag{1}$$

d_i can be expressed using the Euclidean norm

$$d_i = \sqrt{(x - x_i)^2 + (y - y_i)^2 + (z - z_i)^2} \tag{2}$$

in which

$$\begin{cases} x_i = -h(\cos\gamma_i\, r_{11} + \sin\gamma_i\, r_{21}) + g\cos\gamma_i \\ y_i = -h(\cos\gamma_i\, r_{12} + \sin\gamma_i\, r_{22}) + g\sin\gamma_i \\ z_i = -h(\cos\gamma_i\, r_{13} + \sin\gamma_i\, r_{23}) \end{cases} \tag{3}$$

The active and passive joints θ_i and ψ_i, respectively, are expressed as

$$\psi_i = \sin^{-1}\left(\frac{\cos\gamma_i\,(x - x_i) + \sin\gamma_i\,(y - y_i)}{d_i}\right) \tag{4}$$

$$\Theta_i = \sin^{-1}\left(\frac{\sin\gamma_i\,(x - x_i) + \cos\gamma_i\,(y - y_i)}{d_i\cos\psi_i}\right) \tag{5}$$

5 Inverse Dynamics

The principle of virtual work is used to determine the relationship between joint and end-effector forces and torques. The principle of virtual work is described as

$$\delta\mathbf{q}^{\mathrm{T}}\boldsymbol{\tau} + \delta\boldsymbol{x}_p^{\mathrm{T}}\mathbf{F}_p + \sum_i \delta\boldsymbol{x}_i^{\mathrm{T}}\mathbf{F}_i = 0 \tag{6}$$

The 6-dimensional wrench $\mathbf{F}_i$ is the sum of both inertial and applied wrenches around link i's center of mass (CoM). $\mathbf{F}_p$ is denoted as the sum of applied and inertial wrenches around the moving ring's CoM. The wrench applied on the actuators is denoted by $\boldsymbol{\tau}$. $\delta\boldsymbol{x}_p$, $\delta\boldsymbol{x}_i$, and $\delta\mathbf{q}$ are denoted as the virtual displacement and rotation about the center of the moving ring, center of link i, and $\mathbf{q}$, respectively, where $\dot{\mathbf{q}} = [\dot{\theta}_1\ \dot{\theta}_2\ \dot{\theta}_3\ \dot{d}_1\ \dot{d}_2\ \dot{d}_3]^T$ is the

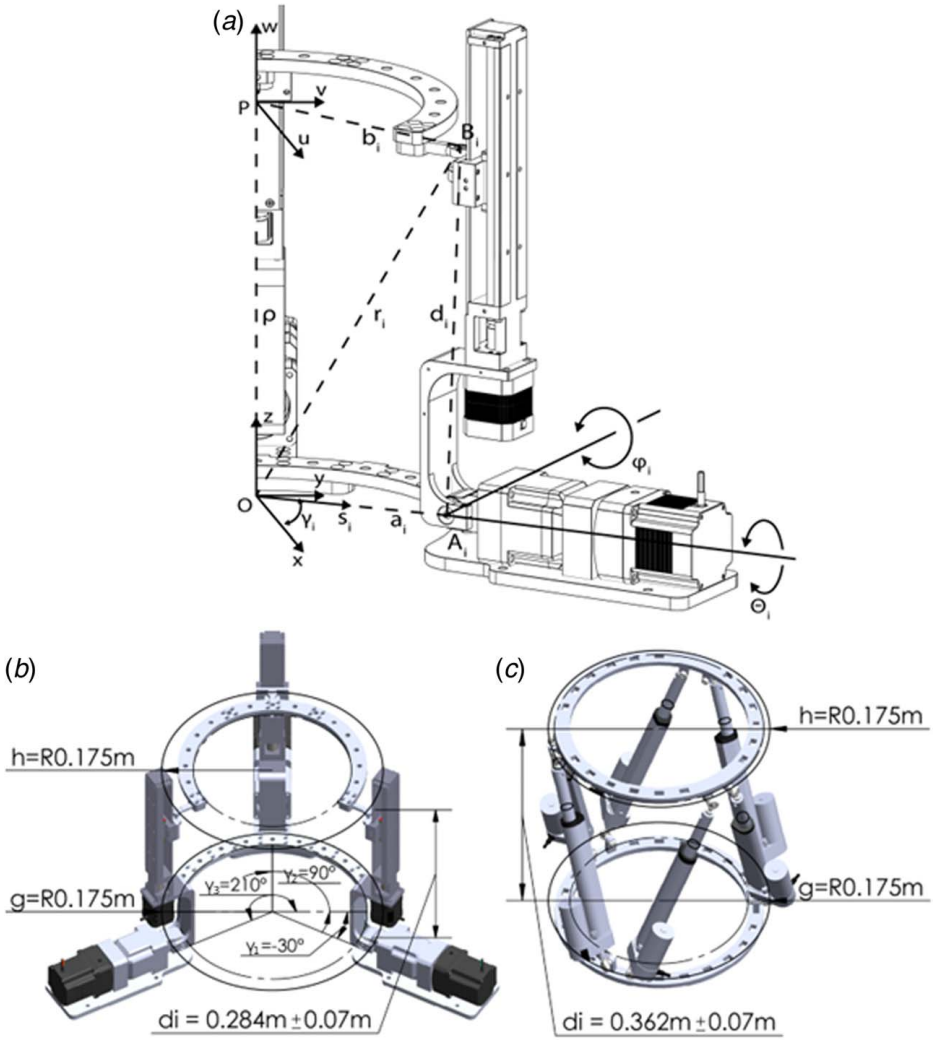

Fig. 3 (*a*) The *i*th arm kinematic variables are shown. The active and passive rotations are denoted by θ_i and φ_i, respectively. (*b*) The CAD model for Robossis with arm angles $\gamma_1 = -30$ deg, $\gamma_2 = 90$ deg, $\gamma_3 = 210$ deg. (*b*, *c*) The CAD models for Robossis and the 3_3 SPS Gough–Stewart platform. *h* and *g* are the moving and fixed rings, respectively. d_i is the linear actuator range. Robossis utilizes a sliding stage linear actuator allowing for a more compact linear actuator while maintaining the same stroke length: ±0.07 m. (c) The arm angle positions for the Gough–Stewart platform moving, and fixed rings are $h\gamma_{1-6}$ = 82.5 deg, 97.5 deg, 202.5 deg, 217.5 deg, 322.5 deg, and 337.5 deg and $g\gamma_{1-6} = 37.5$ deg, 141.5 deg, 157.5 deg, 262.5 deg, 277.5 deg, and 22.5 deg.

joint velocity vector, and $\delta\mathbf{q}$ and $\delta\boldsymbol{x}_p$ are related as

$$\delta\mathbf{q} = \boldsymbol{J}\delta\boldsymbol{x}_p \tag{7}$$

where $\boldsymbol{J}$ denotes the Jacobian matrix. Designating $\boldsymbol{J_i}$ as link i's Jacobian

$$\delta\boldsymbol{x}_i = \boldsymbol{J}_i\delta\boldsymbol{x}_p \tag{8}$$

Solving for $\boldsymbol{\tau}$ provides the necessary motor torque to support a given position and speed of the mechanism

$$\tau = -\boldsymbol{J}^{-\mathrm{T}}\left(\mathbf{F}_p + \sum_i \boldsymbol{J}_i^{\mathrm{T}}\mathbf{F}_i\right) \tag{9}$$

6 Translational and Rotational Workspace Analysis

To understand the performance of Robossis, a comparison with the 3_3-SPS-GSP was made [35]. The 3_3 GSP has the best performance metrics of all the well-known GSP variations [21]. Robossis and the GSP were analyzed in terms of their theoretical translational and rotational workspaces. For both mechanisms, the fixed and moving rings g and h have a radius of 0.175 m (Figs. 3(*b*) and 3(*c*)). The radius is defined as the distance from the center of the ring to the center of the spherical joint. Both mechanisms have a linear actuator stroke length of 0.14 m but have different midrange positions (d_i in Figs. 3(*b*) and 3(*c*)). The linear actuator ranges, d_i, for Robossis and the GSP are 0.214 m–0.354 m and 0.292 m–0.432 m, respectively. For the unconstrained comparison of Robossis and the GSP, the only limit on the inverse kinematic solutions of both mechanisms is the prismatic joint linear actuator range. This approach allows for a comparison of different parallel mechanisms based on their best possible theoretical workspace, not limited by any rotational joint angles.

6.1 Translational Workspace Comparison. The translational workspace was determined by assuming an initial 3D space with a length and width equal to 0.8 m and a height from 0.1 to0.45 m. Each [x, y, z] point in the 3D space was input to the inverse kinematics solution (Eqs. (2)–(5)) to determine if it was within the linear actuator range, d_i. This analysis determines the

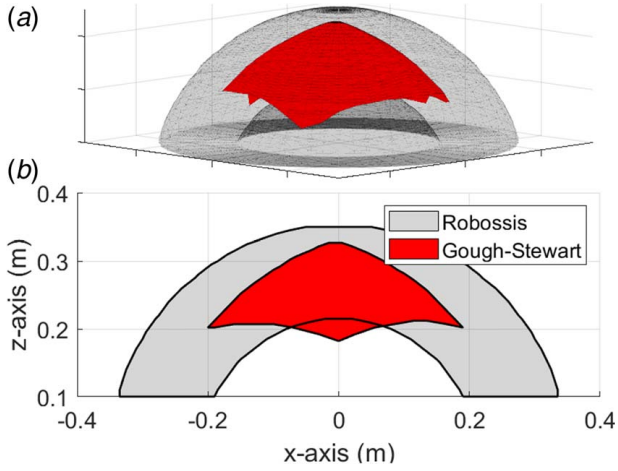

Fig. 4 (*a*) The unconstrained translational workspace of Robossis and the Gough–Stewart platform are overlaid for visual comparison and (*b*) the translational workspaces at $y = 0$ m

translational workspace each mechanism can reach without exceeding the linear actuator range. The results are shown in Fig. 4. Robossis and the GSP have workspace volumes of 4.66E-2 m^3 and 8.53E-3 m^3, respectively. Robossis has a larger workspace due to the nature of the mechanisms. The GSP workspace is the result of the intersection of six spheres, while Robossis is the result of the intersection of three spheres.

6.2 Rotational Workspace Comparison. The rotational workspace was determined by first setting the point P (Fig. 3(*a*)) of the moving platform to be at the midrange position, $[x = 0$ m, $y = 0$ m, $z = 0.284$ m$]$ and $[x = 0$ m, $y = 0$ m, $z = 0.362$ m$]$, for

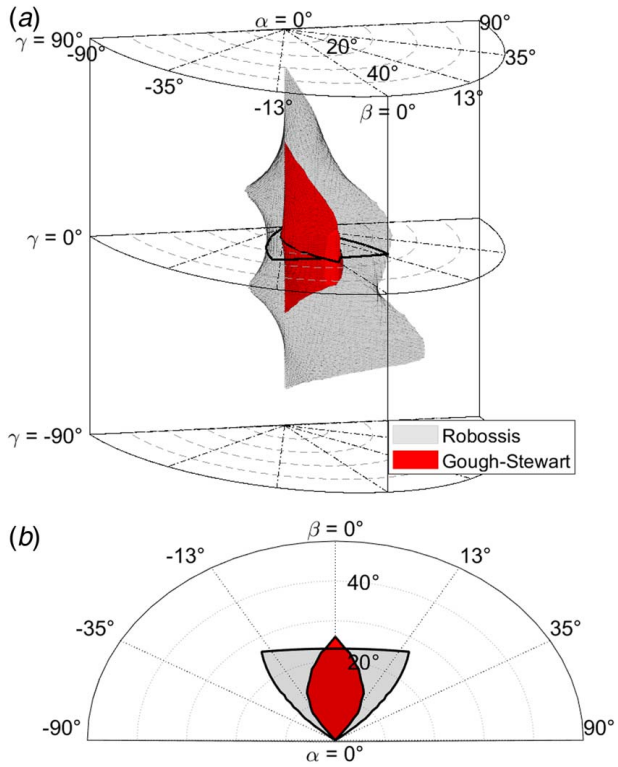

Fig. 5 (*a*) The unconstrained rotational workspace of Robossis and the Gough–Stewart platform in cylindrical coordinates and (*b*) the rotational workspace of Robossis and the Gough–Stewart platform at $\gamma = 0$ deg

Robossis and the GSP, respectively. The Euler angles α, β, and γ, based on the XYZ convention, were then incremented by 1 deg varying from $[-180$ deg, 180 deg$]$. At each step, the position, $[x, y, z, \alpha, \beta, \gamma]$ was input to the inverse kinematics solution (Eqs. (2)–(5)) to determine if the position was within the constraints of the linear actuators. The results are shown in Fig. 5 using cylindrical coordinates $[r, \Theta, z]$, where $r = \alpha$, $\Theta = \beta$, and $z = \gamma$. Due to the nature of cylindrical coordinates, only the positive values of α are shown. Based on Fig. 5, it can be observed that Robossis has a larger rotational workspace than the GSP and provides an advantage in applications requiring large rotational capabilities.

7 Mechanism Analysis Based on the Clinical and Mechanical Requirements

Based on the literature data in Table 2, it is desired to analyze the ability of the GSP and Robossis to meet the mechanical design requirements of femur fracture surgeries. Since 2004 (Table 1), the GSP has been investigated as a possible mechanism for robot-assistive femur fracture surgery, yet there is not currently a commercially available device for this application. This may be, in part, due to the GSP lacking the translational and rotational workspace necessary for clinical applications. To address this concern, we attempt to quantify specific minimum translations and rotations necessary for a device to be used in robot-assisted femur fracture surgery. From the literature, we were able to assign translation and rotation requirements based on the femur fracture malalignment range (Table 2). The maximal reported malalignments in Table 2 were linearly interpolated to create a 3D volumetric malalignment range.

In contrast with the unconstrained workspace in Sec. 6, both Robossis and the SPS-GSP are now also constrained by spherical joints ranging from ± 25 deg in addition to the stroke length of the linear actuators. This provides a comparison of how both mechanisms would perform if manufactured with commercially available parts. The workspaces in Secs. 7.1 and 7.2 show all points the prototypes in Figs. 3(*b*) and 3(*c*) can reach. The mechanical interference limitations on the active and passive revolute joints do not affect the workspace volume and are not included as constraints.

7.1 Rotational Requirements: Malalignment Range. We compare the constrained rotational workspaces of Robossis and the GSP and label the femoral–shaft axis rotational requirement from Table 2. Figure 6(*a*) provides the constrained rotational workspaces for Robossis and the GSP. Figure 6(*b*) provides a 2D slice at $\beta = 0$ deg. Robossis can reach the clinical rotation requirements around all axes while the GSP cannot.

7.2 Translational Requirements: Malalignment Range. The comparison of the constrained translational workspaces of Robossis and the GSP with the malalignment range provides us with a malalignment range workspace in which we will focus on analyzing the performance of Robossis and the GSP.

Figure 7(*a*) provides constrained translational workspaces for Robossis and the GSP. From Fig. 7, Robossis can reach the clinical translational requirement around all axes while the GSP cannot.

7.3 Clinical Load Requirements. The experimentally measured fracture reduction forces from Zhu et al. (Table 2) were used as a minimum required carrying capacity. We conducted a static load-carrying capacity (SLCC) simulation to determine the maximal loads Robossis can support within the malalignment workspace defined in Sec. 7.2. Based on the SLCC methodology in Fig. 8, the design of Robossis requires stepper motors with a nominal torque of at least 1.6 Nm to support the external loads in Table 2.

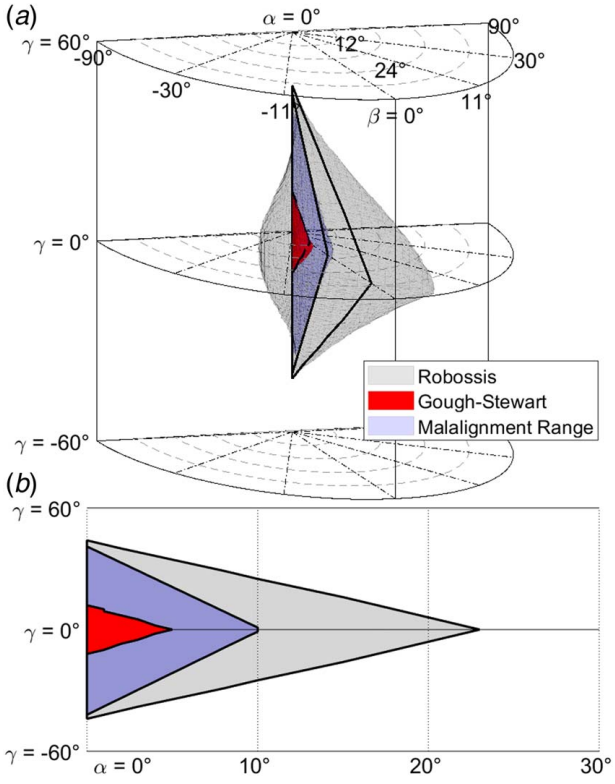

Fig. 6 (*a*) The constrained cylindrical rotational workspaces for the parallel mechanism, Robossis, and the traditional Gough–Stewart platform. Both mechanisms are at their midrange position, [0 m, 0 m, 0.284 m] and [0 m, 0 m, 0.362 m], for Robossis and the GSP, respectively. The malalignment range outlined in Table 3 is shown in blue. (*b*) A 2D slice of the rotational workspace at β = 0 deg.

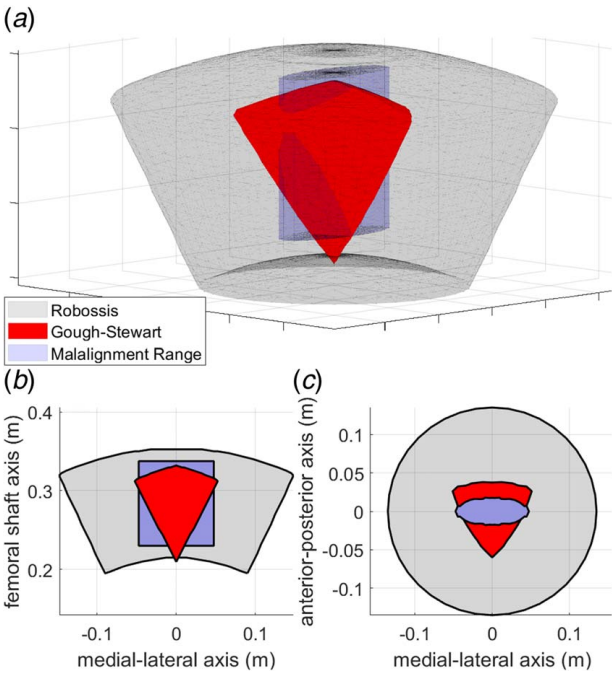

Fig. 7 (*a*) The constrained translational workspaces of Robossis and the Gough–Stewart platform are overlaid for a visual comparison, (*b*) a 2D slice of the translational workspace at *y* = 0 m, and (*c*) a 2D slice of the translational workspace at the midrange position

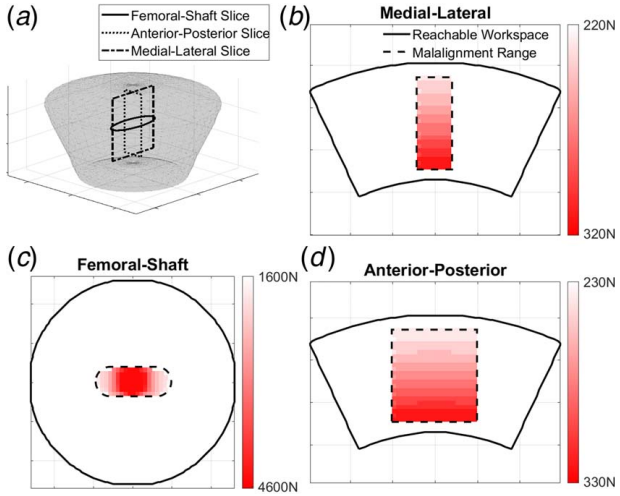

Fig. 8 A static load-carrying capacity simulation was conducted to determine the maximal forces the mechanism can support throughout the maximal malalignment ranges. The nominal torque of the motors used was 0.81 Nm with a 60:1 reduction. (*a*) The three planes that external loads are applied to. (*b*) A 2D slice of the *y*–*z* plane from Fig. 3, with load applied along the medial–lateral axis (*x*-direction). (*c*) A 2D slice of the *x*–*y* plane from Fig 3, with load applied along the femoral–shaft axis (*z*-direction). (*d*) A 2D slice of the *x*–*z* plane from Fig. 3, with load applied along the anterior–posterior axis (negative *y*-direction).

Table 3 Genetic algorithm parameter range and initial conditions

	Parameter range	
Parameter	Minimum	Maximum
γ_1 (deg)	−60	30
γ_2 (deg)	45	90
γ_3 (deg)	150	240
g (m)	0.129	0.200
h (m)	0.129	0.200
Population size of individuals		50
Minimum number of individuals to crossover to next generation		3
Probability of crossover		0.8
Generation limit		500
Constraint tolerance		1e-3

8 Optimization Problem Design and Formulation

Real-world optimization problems tend to be difficult due to the numerous variables as well as insufficient information about the relationship and trends of modifying variables. The genetic algorithm (GA) is population-based, where each population or generation has individuals with randomly assigned values for each parameter [36]. The individuals who are "fittest," that is, perform the best based on the fitness test (objective function), have their parameter values passed onto the next generation [36]. The use of a genetic algorithm for this application is especially important as it robustly searches for a global solution. For optimizing the configuration of Robossis, these individuals have five parameters outlined in Table 3 and shown in Fig. 3(*b*).

8.1 Global Conditioning Index. The GCI was introduced by Gosselin and Angeles [37]. The GCI can be thought of as a single number to describe the isotropy of a parallel mechanism, that is, how uniform and consistent the mechanism will move

throughout the workspace. Since the formulation of the GCI, it has been used as a performance indicator and optimization criterion. The conditioning number (CN) is defined as a measure of the accuracy of the end effector Cartesian velocity

$$\mathrm{CN} = \|\mathbf{J}\| \times \|\mathbf{J}^{-1}\| \tag{10}$$

where $\|\cdot\|$ is the Frobenius norm of the matrix

$$\|\mathbf{J}\| = \sqrt{\mathrm{trace}(\mathbf{J}\mathbf{W}\mathbf{J}^{\mathbf{T}})}, \quad \mathbf{W} = w\mathbf{I}, \quad w = 1/m \tag{11}$$

where m is the dimension of matrix $\mathbf{J}$. This CN is not bound and can range from 1 to infinity. To bound the value between 0 and 1, the inverse is taken and is defined as the conditioning index (CI)

$$\mathrm{CI} = \frac{1}{\mathrm{CN}} \tag{12}$$

The GCI is the integral of the CI over the translational workspace divided by the volume of the workspace

$$n = \frac{\int_W \mathrm{CI}\, dW}{\int_W dW} \tag{13}$$

where W is the parallel mechanism's translational workspace and n is the GCI. As the GCI approaches 1 from 0, the manipulator will have better performance [38]. The CI used to calculate the GCI has been called into question as it is based on the inhomogeneous Jacobian matrix [39]. This criticism stems from the argument that since the Jacobian has both dimensionless and dimensioned units and thus is dimensionally nonhomogeneous, there may not be a physical meaning for the condition number. Tandirci et al. [40] proposed the characteristic length (CL) to create a homogeneous Jacobian. The CL was further studied by Nawratil [41], and it was determined that the CL should be a predefined design constant

$$\mathrm{CL} = R * \sqrt{\frac{2}{3}} \tag{14}$$

where R is the radius of the operation sphere as defined by Nawratil. The CL is then used to create a dimensionally homogeneous Jacobian matrix

$$L = \begin{bmatrix} I & O \\ O & \dfrac{I}{\mathrm{CL}} \end{bmatrix} \tag{15}$$

where L is a 6×6 matrix, I is a 3×3 identity matrix, and O is a 3×3 zero matrix.

$$J_{dh} = JL \tag{16}$$

8.2 Objective Function Description. An objective function (OF) is created to evaluate the fitness of each individual in the population. The OF in Eq. (17) evaluates an individual based on the translational and rotational workspace volumes, the overall force that can be supported, and the GCI

$$O(x) = \max\left(w_1 \frac{n_{\mathrm{in}}}{N_{\mathrm{tot}}} + w_2 \sum_i^{n_R} \frac{R_{i,\mathrm{in}}}{R_{\mathrm{tot}}} + w_3 \sum_i^{n_F} \frac{F_{i,\mathrm{in}}}{F_{\mathrm{tot}}} + w_4 \mathrm{GCI} \right) \tag{17}$$

where n_{in} is the number of points of the desired translational workspace the individual encompasses out of the total number of desired points N_{tot}, and a value of $n_{\mathrm{in}}/N_{\mathrm{tot}} = 1$ indicates the robot configuration can encompass the desired workspace. Similarly, for the rotational workspace, $R_{i,\mathrm{in}}$ is the number of points of the desired rotational workspace the individual encompasses out of the total number of desired points R_{tot}. Due to the nature of parallel mechanisms, the rotational workspace changes in size depending on where the end effector is in the translational workspace. Addressing this point, the points inside the desired workspace $R_{i,\mathrm{in}}/R_{\mathrm{tot}}$ are evaluated at three positions (n_R is set to 3) in the translational workspace: at the (1) midrange position of Robossis and at the (2) maximum and (3) minimum x-position of the medial–lateral malalignment range (Table 2). The x-axis was chosen as this is the largest proportion of variance that is observed. After pulling traction, Robossis would then be attached to assist with the procedure. The action of pulling traction is anticipated to significantly reduce variance in the z-direction (femoral–shaft axis), leaving the x-axis (medial–lateral axis) as the largest axis of variation.

To ensure the individual can meet the forces observed during femur fracture surgery, the dynamics model (Eq. (9)) was used to determine the minimal force the individual can support. It is desired that the minimal force the individual can support is equal to or greater than the maximal force observed during femur fracture repair (Table 2). In Eq. (17), F_{tot} is the maximal force from Table 2 for each direction. $F_{i,\mathrm{in}}$ is the minimal amount of force the individual can support in each direction. The individual was evaluated on the ability to support loads in the x, y, and z directions (n_F is set to 3). For each direction, the SLCC simulation from Fig. 8 was used to determine the minimum guaranteed load within the femur fracture malalignment range. The smallest load recorded from the SLCC is $F_{i,\mathrm{in}}$. $F_{i,\mathrm{in}}/F_{\mathrm{tot}} = 1$ indicates the individual can support all the maximal loads reported in Table 2. The motor torque used to determine the maximal load was 1.6 Nm, the minimum result from the SLCC analysis. Lastly, the GCI was calculated using the homogeneous Jacobian. Weights were used to apply significance to the different parameters ($w_1 - w_4$). Figure 9 depicts the genetic algorithm pipeline used to obtain the optimal parameters for Robossis.

8.3 Single-Objective Genetic Algorithm. Based on the results found by Yoon et al. [42], the GCI decreases as the rotational and translational workspaces increase. This inverse relationship provides a challenge when trying to optimize a mechanism for both parameters. To observe the effects of GCI and workspace size, the weights in the GA were set to only include GCI, and only include $R_{i,\mathrm{in}}$. For maximizing GCI: (a) $w_{1-4} = [0, 0, 0, 1]$. For maximizing the rotational workspace: (b) $w_{1-4} = [0, 1, 0, 0]$. Figure 10 shows the result of the genetic algorithm for maximizing rotational workspace and GCI. The GCI and rotational volume for Robossis appear to have an inverse relationship.

Next, it is desired to have a robot configuration that meets the desired translation and rotation requirements as well as the force requirements (all ratios: $n_{\mathrm{in}}/N_{\mathrm{tot}}$, $R_{i,\mathrm{in}}/R_{\mathrm{tot}}$, $F_{i,\mathrm{in}}/F_{\mathrm{tot}} = 1$). The weights were all initially set to 1: $w_{1-4} = [1, 1, 1, 1]$. After the

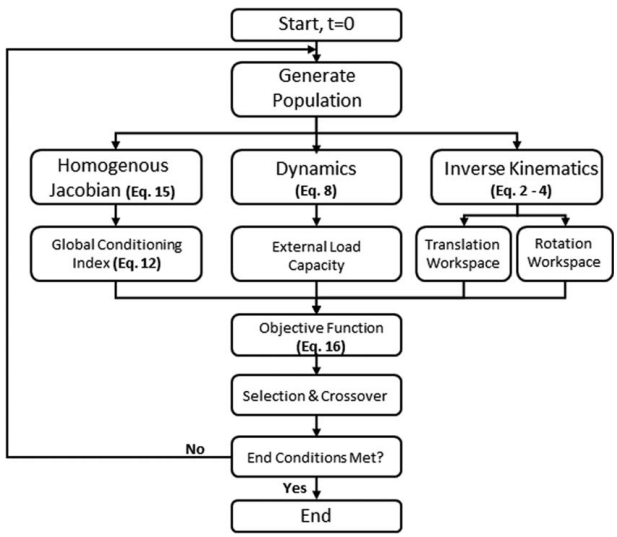

Fig. 9 Overview flowchart depicting the individual steps during the genetic algorithm optimization

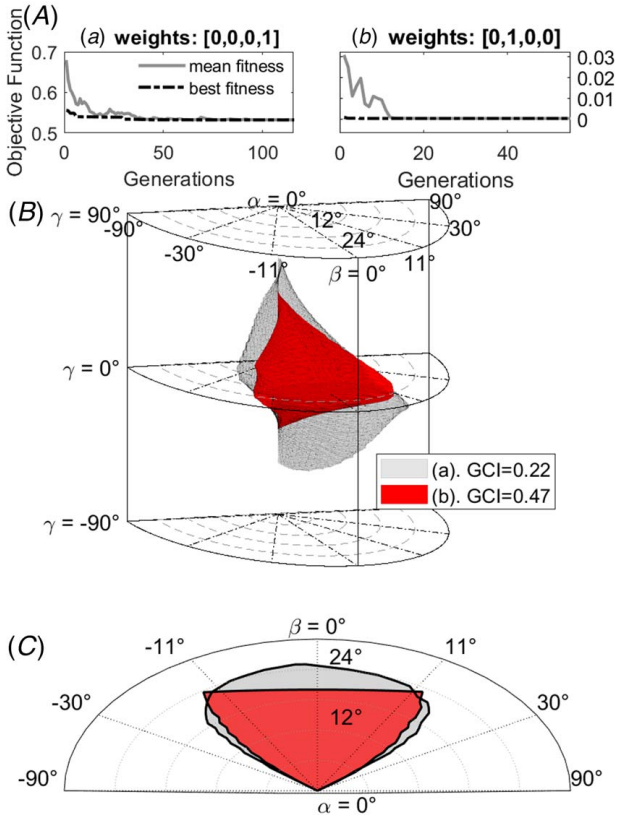

Fig. 10 Five input design parameters of the parallel mechanism, Robossis, were optimized using a single-objective genetic algorithm. (*A*) (a) The objective function with weights: $w_{1-4} = [0, 0, 0, 1]$, and (b) the objective function with weights: $w_{1-4} = [0, 1, 0, 0]$. (*B*) The rotational workspace at [0 m, 0 m, 0.284 m]. The five design parameters obtained from (*A*) were used to determine the rotational workspaces and GCI values. From (*B*) increasing GCI results in decreasing rotational volume and vice versa. (*C*) A 2D slice of the rotational workspace in (*B*) at $\gamma = 0$ deg.

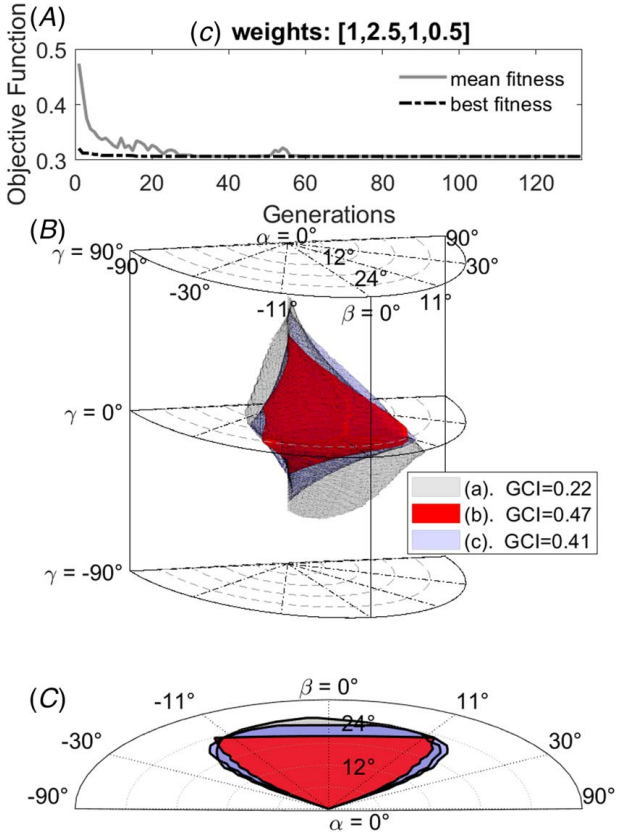

Fig. 11 (*A*) The objective function with weights: (c) $w_{1-4} = [0, 0, 0, 1]$. (*B*) The rotational workspace at [0 m, 0 m, 0.284 m]. The objective function (c) is compared to the two objective functions (a) and (b) from Fig. 10 (*C*) A 2D slice of the rotational workspace in (*C*) at $\gamma = 0$ deg.

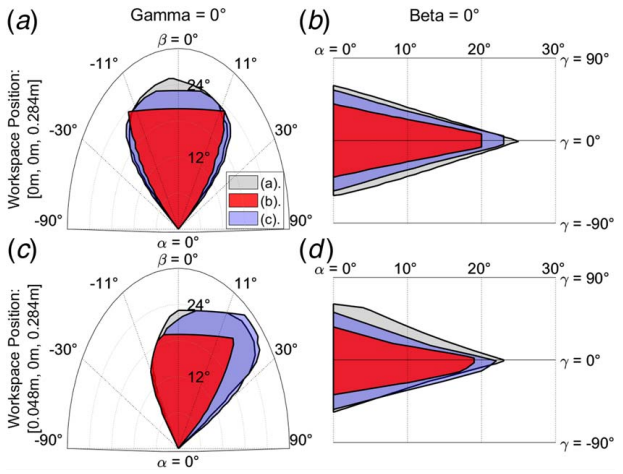

Fig. 12 The three different individuals generated by the genetic algorithm (*a–c*) have their rotational workspace compared at various end effector positions. (*a–b*) A 2D slice of the rotational workspace at the base position: [0 m, 0 m, 0.284 m] at $\gamma = 0$ deg and $\beta = 0$ deg, respectively. (*c–d*) A 2D slice of the rotational workspace at the edge of the medial–lateral femur fracture malalignment range [0.048 m, 0 m, 0.284 m].

genetic algorithm was run, if a ratio did not equal 1, the weight for that ratio was altered, and the GA was run again. The final weights for the GA were $[w_1 = 1, w_2 = 2.5, w_3 = 1, w_4 = 0.5]$. Figure 11 compares the results of the three GA optimizations.

For parallel mechanisms, it is understood that the size of the rotational workspace decreases as the end effector moves from the midrange position. Figure 12 displays the rotational workspace at two end effector positions, the midrange position and the edge of the medial–lateral femur fracture malalignment range. The configurations from (a) and (c) can encompass all the requirements: n_{in}/N_{tot}, $R_{i,in}/R_{tot}$, $F_{i,in}/F_{tot} = 1$, as seen in the objective function parameter outputs in Table 4.

Table 4 includes the results of the GA for the three optimizations performed: (a) maximize rotations, (b) maximize GCI, and (c) meet all the OF requirements. In addition to the three GA optimizations, the current configuration of Robossis is shown for a comparison. Based on the information presented in Table 4, no configuration is the best in all areas of analysis. The GA result (c) meets all the objective function criteria and has a GCI of 0.407. Compared to the current Robossis design, the GA result (c) has a 29% decrease in translational workspace volume, a 38% increase in rotational volume, and a 7.3% decrease in GCI.

9 Experimental Testing

Experimental testing was conducted to study the accuracy, precision, and reliability under anatomically relevant loads. Three OptiTrack Flex-13 (NaturalPoint, Corvallis, OR) motion capture cameras were used alongside the MOTIVE software to track the 6-DoF motion of Robossis during the experimental testing using IR reflective markers (Fig. 13(*a*)). The testing was segmented into two parts: complex movements while under varying external forces (Fig. 13(*b*)) and repetitive precision testing under constant

Table 4 Comparison of results using the single-objective genetic algorithm with the current design of Robossis

GA weights		GA optimization (a) [0,0,0,1]	GA optimization (b) [0,1,0,0]	GA optimization (c) [1,2.5,1,0.5]	Current Robossis design
γ_1 (deg)		−31.81	−1.07	−32.11	−30
γ_2 (deg)		88.19	47.29	87.88	90
γ_3 (deg)		208.19	165.92	207.89	210
h (m)		0.200	0.131	0.150	0.175
g (m)		0.182	0.131	0.130	0.175
Objective function parameter outputs					
$\frac{n_{in}}{N_{tot}}$		1	1	1	1
$\frac{R_{i,in}}{R_{tot}}$		0.96	1	1	0.98
$\frac{F_{i,in}}{F_{tot}}$		1	1	1	1
GCI		0.468	0.217	0.407	0.439
Mechanism performance at midrange position [0 m, 0 m, 0.284 m, 0 deg, 0 deg, 0 deg]					
Translational volume (m^3)		4.76E-3	6.48E-3	4.63E-3	6.49E-3
Rotational volume (rad^3)		1.80E-2	3.57E-2	2.68E-2	1.94E-2
External load limits					
F_x (N)		518	249	519	517
F_y (N)		553	613	552	564
F_z (N)		4571	2436	4569	4581
Rotational limits					
α (deg)	Min.	−20.51	−23.18	−24.14	−21.74
	Max.	20.47	24.94	23.77	23.34
β (deg)	Min.	−23.46	−22.60	−23.87	−22.16
	Max.	23.35	22.52	23.86	22.17
γ (deg)	Min.	−40.23	−60.79	−55.87	−44.46
	Max.	40.24	60.79	55.86	44.45

Note: GA weight labels: the arm angle locations shown in Fig. 3(*b*): γ_1, γ_2, and γ_3; moving ring: h; and fixed ring: g.

load (Fig. 13(*c*)). The error metric used was the Euclidean distance between the theoretical position of the robot and the actual position recorded by OptiTrack.

9.1 Repetitive Precision Testing. To evaluate if there is an accruing error, repetitive testing was conducted. Robossis was commanded to move in isolated repetitive motions to gauge the accuracy and reliability of the mechanism. An isolated repetitive motion is defined as a 1D movement along each of the 6-DoFs (x, y, z, α, β, γ). The experimental results are displayed in Fig. 14. A one-sided t test was used to determine if the experimental results were less than the OptiTrack accuracy threshold of 0.088 mm. All isolated repetitive motion errors were significantly less than OptiTrack's accuracy threshold ($p < 0.05$).

9.2 Complex Movements. During the proposed use case, femur fracture repair, the movements of the robot will not be simple in nature, and the robot will move simultaneously along multiple axes. To evaluate the performance of Robossis, the robot was

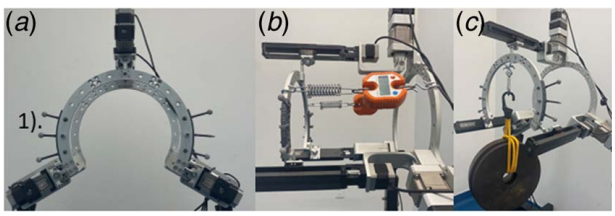

Fig. 13 Experimental testing configuration: (*a*) (1) reflective markers attached to the moving ring to track the position of Robossis, (*b*) a variable load is achieved with springs attached to the moving and fixed rings, and (c) a static load is created by hanging weights from the moving ring

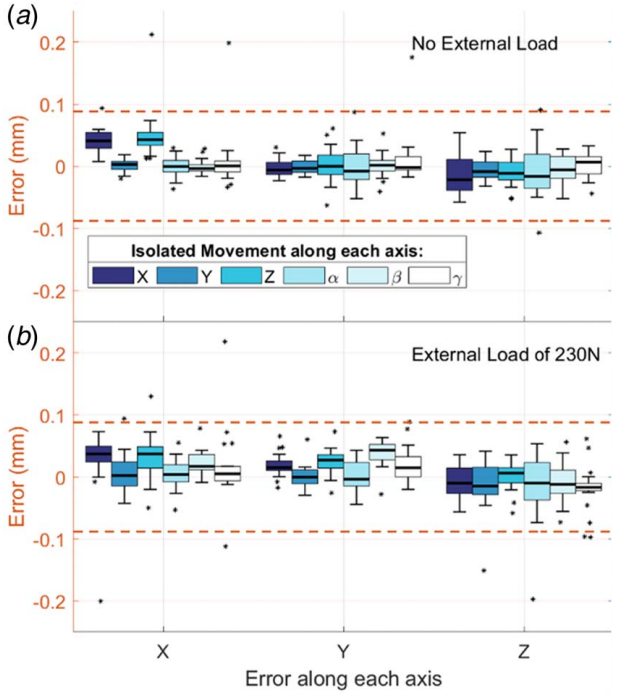

Fig. 14 Robossis was commanded to move in isolated repetitive motions. OptiTrack's MOTIVE recording software was measured to have an accuracy of 0.088 mm, shown as the dotted lines. The movements along the *x*, *y*, and *z*, axes and α, β, and γ rotation axes were 10 mm and 10 deg, respectively. Each movement was performed 20 times. (*a*) Isolated repetitive movements with no external load. (*b*) Isolated repetitive movements with an external load of 230 N.

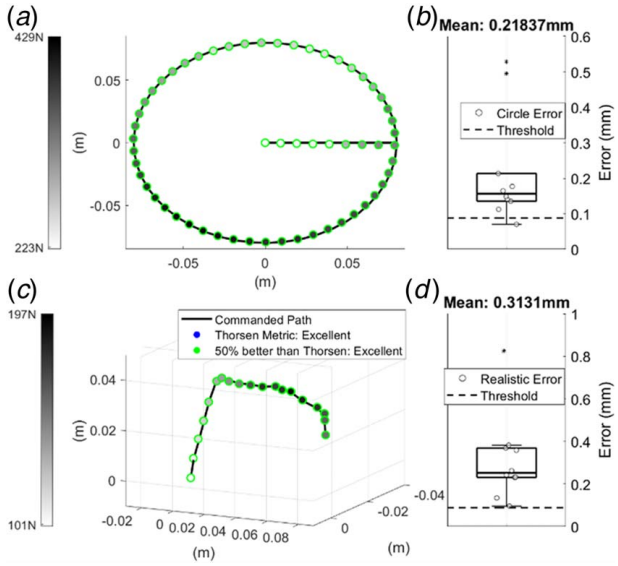

Fig. 15 Robossis was commanded to move in complex motions while under external load, each trajectory was repeated 10 times. Robossis maintained accuracy better than the Thorsen metric: excellent (<1 cm and <5 deg error) and 50% of the Thorsen: excellent (<0.5 cm and <2.5 deg error) throughout all movements. (*a*, *c*) Robossis was tasked to move along 2D and 3D trajectories while experiencing loads from 223–429 N and from 101–197 N, respectively. (*b*, *d*) Average trajectory completion error. Springs were attached to both the moving and fixed rings to allow for changing forces throughout the movement.

commanded to move along two paths: a 2D path and a 3D path. The first path was a circle with a varying external load, as seen in Fig. 15(*a*). The second path was along a 3D trajectory (Fig. 15(*c*)). Both experiments had an average trajectory error of less than 1 mm (Figs. 15(*b*)–15(*d*)). Additionally, both experiments were able to maintain the clinical criteria of at least 50% better than the Thoresen Metric "Excellent," as shown by the green markers in Fig. 15.

10 Discussion

Based on our analysis and work, the need for improved clinical outcomes in femur fracture surgeries, the limitations with traditional parallel mechanisms for this application, an optimized solution of Robossis based on the femur fracture design criteria, and experimental force testing to evaluate the precision of Robossis has been demonstrated. The GSP is not able to meet the workspace limits outlined by our preliminary femur fracture malalignment range; this may be one of the reasons the GSP has not been used for femur fracture surgeries. Based on the static load-carrying capacity, Robossis needs motors capable of generating 1.6 Nm of torque; these motors can be adapted to the design without affecting the overall workspace. The genetic algorithm was able to find a solution to meet all the desired criteria of the objective function, increasing the rotational workspace volume by 38%. This result was only possible due to a 29% decrease in the translational workspace and a 7.3% decrease in GCI, as seen in Table 4. Further analysis and discussion may be necessary to determine if this tradeoff is overall beneficial.

The limitations of this study are the lack of literature-reported values on the necessary clinical and mechanical design criteria. The design criteria are based on the femur fracture malalignment range, which provides an estimate of the translational and rotational movements during femur fracture reduction surgery but does not give the exact movement ranges during surgery. In future work, it would be pertinent to design a musculoskeletal model to determine how the femur fragments can be manipulated before causing soft tissue damage and to record translational and rotational ranges during femur fracture repair surgeries. The goal would be to have an exact fracture reduction range similar to Lei and Wang's work on pelvic fractures [43]. This would allow for a more accurate description of the workspace a robot must have to be used for femur fracture repair surgery and provide foresight on how much clinicians can manipulate the femur fragments before risking soft tissue damage.

11 Conclusion

Femur fracture surgery requires both large forces and rotations to reduce the fracture. Currently, these forces are generated manually by surgeons with the assistance of traction tables. We propose a parallel mechanism, Robossis, which is shown to be capable of generating the required forces, as well as meeting the clinical requirements to improve patient outcomes during femur fracture surgeries. In this study, we investigated the theoretical workspace and force generation limits and optimized the design to satisfy the mechanical and clinical design criteria. Through this analysis and optimization, it has been concluded that Robossis has the potential to improve clinical outcomes and reduce the chance of reoperations as a robot-assistive surgical device.

Funding Data

- The work presented in this paper was supported by the National Science Foundation (NSF) under Grant Nos. 2141099 and 2226489, and by the New Jersey Health Foundation (NJHF) under Grant No. PC 62-21.

Conflict of Interest

There are no conflicts of interest.

Data Availability Statement

The datasets generated and supporting the findings of this article are obtainable from the corresponding author upon reasonable request.

References

[1] Gomes, P., 2011, "Surgical Robotics: Reviewing the Past, Analysing the Present, Imagining the Future," Rob. Comput. Integr. Manuf., **27**(2), pp. 261–266.
[2] Ng, A. T. L., and Tam, P. C., 2014, "Current Status of Robot-Assisted Surgery," Hong Kong Med. J., **20**(3), pp. 241–250.
[3] Cho, K.-J., Seon, J.-K., Jang, W.-Y., Park, C.-G., and Song, E.-K., 2019, "Robotic Versus Conventional Primary Total Knee Arthroplasty: Clinical and Radiological Long-Term Results With a Minimum Follow-Up of Ten Years," Int. Orthop., **43**(6), pp. 1345–1354.
[4] Lundin, N., Huttunen, T. T., Enocson, A., Marcano, A. I., Felländer-Tsai, L., and Berg, H. E., 2021, "Epidemiology and Mortality of Pelvic and Femur Fractures—A Nationwide Register Study of 417,840 Fractures in Sweden Across 16 Years: Diverging Trends for Potentially Lethal Fractures," Acta Orthop., **92**(3), pp. 323–328.
[5] Honeycutt, M., W, Cox, K., Cox, W. T., Delgado, G., and Brewer, J., 2019, "The Effect of Intramedullary Nail Entry Point on Postoperative Femoral Shaft," AM19: Hip/Femur, PAPER #100.
[6] Zhu, Q., Liang, B., Wang, X., Sun, X., and Wang, L., 2016, "Force–Torque Intraoperative Measurements for Femoral Shaft Fracture Reduction," Comput. Assist. Surg., **21**(sup1), pp. 37–44.
[7] Seide, K., Faschingbauer, M., Wenzl, M. E., Weinrich, N., and Juergens, C., 2004, "A Hexapod Robot External Fixator for Computer Assisted Fracture Reduction and Deformity Correction," Int. J. Med. Rob., **1**(1), pp. 64–69.
[8] Kim, W. Y., Joung, S., Park, H., Park, J.-O., and Ko, S. Y., 2022, "Human-Robot-Robot Cooperative Control Using Positioning Robot and 1-DOF Traction Device for Robot-Assisted Fracture Reduction System," Proc. Inst. Mech. Eng. H, **236**(5), pp. 697–710.
[9] Ye, R., Chen, Y., and Yau, W., 2012, "A Simple and Novel Hybrid Robotic System for Robot-Assisted Femur Fracture Reduction," Adv. Rob., **26**(1–2), pp. 83–104.
[10] Mukherjee, S., Rendsburg, M., and Xu, W. L., 2005, "Surgeon-Instructed, Image-Guided and Robot-Assisted Long Bone Fractures Reduction," 1st

International Conference on Sensing Technology, Palmerston North, New Zealand, Nov. 21–23, pp. 78–84.
[11] Wang, J., Han, W., and Lin, H., 2013, "Femoral Fracture Reduction With a Parallel Manipulator Robot on a Traction Table," Int. J. Med. Robotics Comput. Assist. Surg., **9**(4), pp. 464–471.
[12] Wang, T., Li, C., Hu, L., Tang, P., Zhang, L., Du, H., Luan, S., Wang, L., Tan, Y., and Peng, C., 2014, "A Removable Hybrid Robot System for Long Bone Fracture Reduction," Biomed. Mater. Eng., **24**(1), pp. 501–509.
[13] Du, H., Hu, L., Li, C., Wang, T., Zhao, L., Li, Y., Mao, Z., et al., 2015, "Advancing Computer-Assisted Orthopaedic Surgery Using a Hexapod Device for Closed Diaphyseal Fracture Reduction," Int. J. Med. Rob. Comput. Assist. Surg., **11**(3), pp. 348–359.
[14] Dagnino, G., Georgilas, I., Morad, S., Gibbons, P., Tarassoli, P., Atkins, R., and Dogramadzi, S., 2017, "Image-Guided Surgical Robotic System for Percutaneous Reduction of Joint Fractures," Ann. Biomed. Eng., **45**(11), pp. 2648–2662.
[15] Essomba, T., and Nguyen Phu, S., 2021, "Kinematic Analysis and Design of a Six-Degrees of Freedom 3-RRPS Mechanism for Bone Reduction Surgery," ASME J. Med. Devices, **15**(1), p. 011101.
[16] Jamwal, P. K., Hussain, S., and Ghayesh, M. H., 2021, "Intrinsically Compliant Parallel Robot for Fractured Femur Reduction: Mechanism Optimization and Control," Rob. Auton. Syst., **141**, p. 103787.
[17] Lee, S., Joung, S., Ha, H.-G., Lee, J.-H., Park, K.-H., Kim, S., Nam, K., et al., 2022, "3D Image-Guided Robotic System for Bone Fracture Reduction," IEEE Rob. Autom. Lett., **7**(2), pp. 4353–4360.
[18] Abedinnasab, M. H., Farahmand, F., and Gallardo-Alvarado, J., 2017, "The Wide-Open Three-Legged Parallel Robot for Long-Bone Fracture Reduction," ASME J. Mech. Rob., **9**(1), p. 015001.
[19] Abedinnasab, M. H., Gallardo-Alvarado, J., Tarvirdizadeh, B., and Farahmand, F., 2016, "Sliding-Mode Tracking Control of the 6-DOF 3-Legged Wide-Open Parallel Robot," *Parallel Manipulators: Design, Applications and Dynamic Analysis*, Nova Science Publishers, Inc., Hauppauge, NY, pp. 143–166.
[20] Abedinnasab, M. H., Farahmand, F., Tarvirdizadeh, B., Zohoor, H., and Gallardo-Alvarado, J., 2017, "Kinematic Effects of Number of Legs in 6-DOF UPS Parallel Mechanisms," Robotica, **35**(12), pp. 2257–2277.
[21] Abedinnasab, M. H., Yoon, Y.-J., and Zohoor, H., 2012, "Exploiting Higher Kinematic Performance—Using a 4-Legged Redundant PM Rather Than Gough-Stewart Platforms," *Ser. Parallel Rob. Manipul.-Kinemat., Dyn., Control Optim.*, S. Küçük, ed., IntechOpen, London, UK, pp. 43–66.
[22] Alruwaili, F., Saeedi-Hosseiny, M. S., Clancy, M., McMillan, S., Iordachita, I. I., and Abedin-Nasab, M. H., 2022, "Experimental Evaluation of a 3-Armed 6-DOF Parallel Robot for Femur Fracture Surgery," J. Med. Rob. Res., **07**(04), p. 2241009.
[23] Saeedi-Hosseiny, M. S., Alruwaili, F., Patel, A. S., McMillan, S., Iordachita, I. I., and Abedin-Nasab, M. H., 2023, "Spatial Detection of the Shafts of Fractured Femur for Image-Guided Robotic Surgery," 2021 43rd Annual International Conference of the IEEE Engineering in Medicine & Biology Society (EMBC), Virtual, Nov. 1–5, IEEE, pp. 3301–3304.
[24] Alruwaili, F., Saeedi-Hosseiny, M. S., Guzman, L., McMillan, S., Iordachita, I. I., and Abedin-Nasab, M. H., 2022, "A 3-Armed 6-DOF Parallel Robot for Femur Fracture Reduction: Trajectory and Force Testing," 2022 International Symposium on Medical Robotics (ISMR), Atlanta, GA, Apr. 13–15, IEEE, pp. 1–6.
[25] Saeedi-Hosseiny, M. S., Alruwaili, F., McMillan, S., Iordachita, I., and Abedin-Nasab, M. H., 2021, "A Surgical Robotic System for Long-Bone Fracture Alignment: Prototyping and Cadaver Study," IEEE Trans. Med. Rob. Bionics, **4**(1), pp. 172–182.
[26] Annappa, R., Mittal, H., Kamath, S. U., Rai, S., Suresh, P. K., and Mohammed, N., 2018, "Rotational Malalignment After Intramedullary Fixation of Trochanteric Fractures," J. Clin. Diagn. Res., **12**(12), pp. 5–8.
[27] Kim, J.-W., Oh, C.-W., Oh, J.-K., Park, I.-H., Kyung, H.-S., Park, K.-H., Yoon, S.-D., and Kim, S.-M., 2017, "Malalignment After Minimally Invasive Plate Osteosynthesis in Distal Femoral Fractures," Injury, **48**(3), pp. 751–757.
[28] Gugenheim, J. J., Probe, R. A., and Brinker, M. R., 2004, "The Effects of Femoral Shaft Malrotation on Lower Extremity Anatomy," J. Orthop. Trauma, **18**(10), pp. 658–664.
[29] Yu, C. K., Singh, V. A., Mariapan, S., and Chong, S. T. B., 2007, "Antegrade Versus Retrograde Locked Intramedullary Nailing for Femoral Fractures: Which Is Better?," Eur. J. Trauma Emergency Surg., **33**(2), pp. 135–140.
[30] McDowell, M. A., Fryar, C. D., Ogden, C. L., and Flegal, K. M., 2008, "Anthropometric Reference Data for Children and Adults: United States, 2003–2006," Natl. Health Stat. Rep., **10**(1–45), p. 5.
[31] Braten, M., Terjesen, T., and Rossvoll, I., 1993, "Torsional Deformity After Intramedullary Nailing of Femoral Shaft Fractures. Measurement of Anteversion Angles in 110 Patients," J. Bone Joint Surg. Br., **75**(5), pp. 799–803.
[32] Citak, M., Suero, E. M., O'Loughlin, P. F., Arvani, M., Hüfner, T., Krettek, C., and Citak, M., 2011, "Femoral Malrotation Following Intramedullary Nailing in Bilateral Femoral Shaft Fractures," Arch. Orthop. Trauma Surg., **131**(6), pp. 823–827.
[33] Lowe, J., Alhandi, A., Manoharan, A., Ouellette, E., Kaimrajh, D., Milne, E., and Latta, L., 2022, "Axial and Rotational Malreduction (Golf Club Deformity) in Distal Femur Fractures," J. Orthop. Trauma, **36**(10), pp. 515–518.
[34] Gösling, T., Westphal, R., Faülstich, J., Sommer, K., Wahl, F., Krettek, C., and Hufner, T., 2006, "Forces and Torques During Fracture Reduction: Intraoperative Measurements in the Femur," J. Orthop. Res., **24**(3), pp. 333–338.
[35] Dasgupta, B., and Mruthyunjaya, T., 2000, "The Stewart Platform Manipulator: A Review," Mech. Mach. Theory, **35**(1), pp. 15–40.
[36] de Jong, K., 1988, "Learning With Genetic Algorithms: An Overview," Mach. Learn., **3**(2), pp. 121–138.
[37] Gosselin, C., and Angeles, J., 1991, "A Global Performance Index for the Kinematic Optimization of Robotic Manipulators," ASME J. Mech. Des., 113(3), pp. 220–226.
[38] Küçük, S., and Bingül, Z., 2003, "Robot Workspace Optimization Based on the Global Conditioning Index," IFAC Proc. Vol., **36**(7), pp. 117–122.
[39] Doty, K. L., Melchiorri, C., and Bonivento, C., 1993, "A Theory of Generalized Inverses Applied to Robotics," Int. J. Rob. Res., **12**(1), pp. 1–19.
[40] Tandirci, M., Angeles, J., and Ranjbaran, F., 1992, "The Characteristic Point and the Characteristic Length of Robotic Manipulators," International Design Engineering Technical Conferences and Computers and Information in Engineering Conference, Scottsdale, AZ, Sept. 13–16, American Society of Mechanical Engineers, pp. 203–208.
[41] Nawratil, G., 2007, "New Performance Indices for 6R Robots," Mech. Mach. Theory, **42**(11), pp. 1499–1511.
[42] Yoon, J. W., Ryu, J., and Hwang, Y.-K., 2010, "Optimum Design of 6-DOF Parallel Manipulator With Translational/Rotational Workspaces for Haptic Device Application," J. Mech. Sci. Technol., **24**(5), pp. 1151–1162.
[43] Lei, J., and Wang, J., 2023, "Orientation Workspace Analysis and Parameter Optimization of 3-RRPS Parallel Robot for Pelvic Fracture Reduction," ASME J. Mech. Rob., **15**(5), p. 051003.